Flow in the nose region and annular film around a Taylor bubble rising through vertical columns of stagnant and flowing Newtonian liquids

S. Nogueira[a, b], M.L. Riethmuler[b], J.B.L.M. Campos[a], A.M.F.R. Pinto[a, *]

[a] *Centro de Estudos de Fenómenos de Transporte, Departamento de Engenharia Química, Faculdade de Engenharia da Universidade do Porto, Rua Dr. Roberto Frias, 4200-465 Porto, Portugal*

[b] *von Kárman Institute for Fluid Dynamics, Chaussée de Waterloo, 72B-1640 Rhode Saint Genèse, Belgium*

Received 15 March 2005; received in revised form 19 July 2005; accepted 29 July 2005
Available online 19 September 2005

Abstract

The flow in the nose region and in the annular film around individual Taylor bubbles rising through stagnant and co-current vertical columns of liquid were studied, employing particle image velocimetry (PIV) and pulsed shadowgraphy techniques (PST) at the same time. The combined techniques enabled simultaneous determination of the bubble shape and the velocity profiles in the liquid film. Experiments were performed with water and aqueous glycerol solutions in a wide range of viscosities (1×10^{-3} Pa s $< \mu <$ 1.5 Pa s), in an acrylic column of 32 mm ID.

Values for the distance ahead of the nose in which the flow is disturbed by the presence of the bubble are presented for the conditions studied. The bubble shapes in the nose region are compared with Dumitrescu's shape for potential flow. The velocity profiles show that after the nose region the liquid begins to accelerate downwards, and at a certain distance from the bubble nose the velocity profile and the liquid film thickness stabilise. The liquid film acquires characteristics of a free-falling film. Values of the developing length and film thickness are reported for the experimental conditions studied. Average velocity profiles in the fully developed film are also presented. A critical Reynolds number of around 80 (based on the mean absolute velocity in the liquid film and on the film thickness) is reported for the transition from laminar to turbulent regime. Shear stress profiles (in the fully developed film) are also provided.

The data reported are relevant for the validation of numerical codes in slug flow.

Keywords: Fluid mechanics; Multiphase flow; Slug flow; Bubble; Films; Particle image velocimetry (PIV)

1. Introduction

Slug flow is a two-phase flow pattern observed when gas and liquid flow simultaneously in a pipe over a determined range of flow rates and is characterised by long bullet-shaped bubbles, also called Taylor bubbles or gas slugs, which occupy nearly the entire cross-section of the pipe. The liquid moves around the bubbles in a thin film and in the bulk between successive bubbles. The liquid moving around the bubble expands at the rear of the bubble, inducing a liquid wake.

This type of flow is found in many practical applications, such as: gas absorption units, nuclear reactors, oil–gas pipelines, steam boilers, heat exchangers and air-lift reactors. A great amount of research has been devoted to the study of this flow pattern since the early 1940s (Dumitrescu, 1943; Moissis and Griffith, 1962; Nicklin et al., 1962; White and Beardmore, 1962; Brown, 1965; Collins et al., 1978; Fernandes et al., 1983; Campos and Guedes de Carvalho, 1988; Mao and Dukler, 1991; Pinto and Campos, 1996; Pinto et al., 1998, 2001). A complete review of this topic is given by Fabre and Liné (1992).

In a slugging column with gas and liquid flowing in co-current conditions, the flow field is extremely complex.

* Corresponding author. Tel.: +351 22 508 1675; fax: +351 22 508 1449.
E-mail addresses: nogueira@fe.up.pt (S. Nogueira), riethmuller@vki.ac.be (M.L. Riethmuler), jmc@fe.up.pt (J.B.L.M. Campos), apinto@fe.up.pt (A.M.F.R. Pinto).

A detailed study of the entire flow field around an individual Taylor bubble is a fundamental step towards a reliable hydrodynamic understanding and simulation of this complex two-phase flow.

In the literature, there are some doubts concerning the velocity and shear stress boundary conditions at the gas–liquid interface. Experiments performed by Mao and Dukler (1991) using intrusive techniques, showed that a liquid film of constant thickness is never reached. Nicklin et al. (1962) observed a stabilised film velocity and thickness below a certain distance from the bubble nose. Accurate velocity profile measurements in the liquid surrounding the bubble are needed to dispel these uncertainties. None of the model predictions on the velocity field around the Taylor bubble has been experimentally validated since there is a lack of velocity data, mainly in the annular liquid film.

Polonsky et al. (1999) studied the motion of an isolated gas slug rising in a vertical pipe filled with water for different liquid flow rates. They used an interlaced image technique to perform particle image velocimetry (PIV) measurements around the bubble nose. van Hout et al. (2002) also performed PIV measurements in stagnant water slug flow for air–water systems. In both studies the authors determined the shape of the Taylor bubble and the velocity field separately. They had problems to accurately determine the velocity fields in the liquid film and in the near- wake region using this technique. Bugg and Saad (2002) studied the flow around a Taylor bubble rising in a viscous solution, sketching the bubble shape by hand directly from the PIV image. This technique is not sufficiently accurate to obtain the velocity field close to the interface or the bubble shape.

In the present study, a recent non-intrusive technique combining PIV and pulsed shadow techniques (PST) was applied to characterise the flow in the nose region and in the annular film around the Taylor bubble. Nogueira et al. (2003) described this simultaneous technique in detail. Bubble shapes, velocity profiles in the region ahead of the nose, as well as velocity fields and shear stress profiles in the liquid film, were obtained for individual bubbles rising in a 32 mm ID vertical tube, in stagnant and co-current flow conditions. Experiments were performed for a wide range of liquid viscosity, $(1 \times 10^{-3}\,\mathrm{Pa\,s} < \mu < 1.5\,\mathrm{Pa\,s})$.

2. Experimental set-up and techniques

2.1. Facility

The experimental study focused on describing the flow field ahead of and around a single Taylor bubble rising in a vertical column with stagnant and co-current liquid. The velocity fields were obtained by simultaneously applying PIV and PST. The experimental set-up is sketched in Fig. 1 and is described in detail by Nogueira et al. (2003).

The experiments were performed in a transparent acrylic column, 6-m in height and 0.032-m internal diameter. The test section was located near the top of the tube to avoid entrance effects and to ensure a stabilised flow (Moissis and Griffith, 1962). A transparent box with plane faces surrounded the test section (0.5 m × 0.12 m × 0.11 m) and was filled with the same study liquid in order to minimise the optical distortion. This box does not completely eliminate the optical distortion, in particular near the tube wall. Calibration images of a very dense scale placed inside the tube filled with liquid show no optical distortion at 0.5 mm from the tube wall and an extremely low radial distortion between the wall and 0.5 mm, which has a non-significant impact on the accuracy of the results.

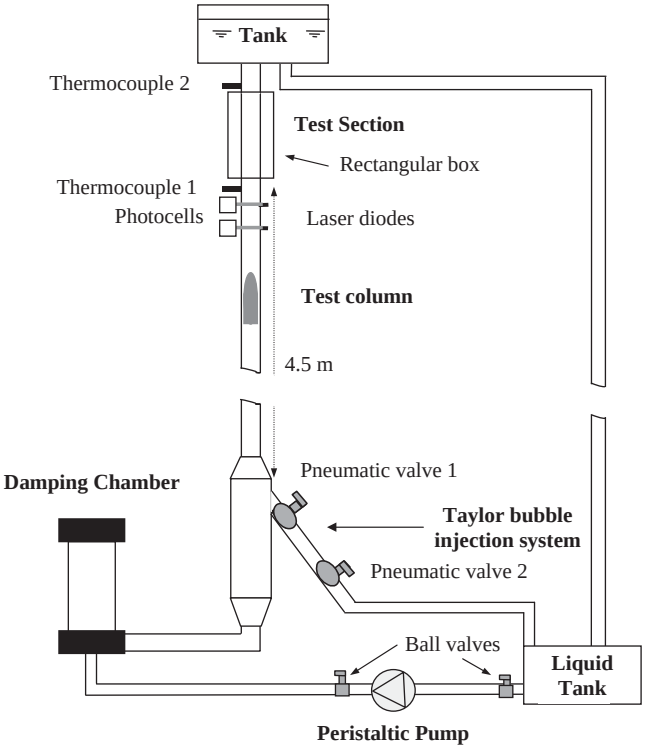

Fig. 1. Experimental set-up.

The individual Taylor bubbles were generated and injected at the bottom of the column by manipulating valves 1 and 2 (Fig. 1). The volume of air used in these experiments ranged from $40 \times 10^{-6}\,\mathrm{m}^3$ to $265 \times 10^{-6}\,\mathrm{m}^3$.

For the experiments in co-current flow conditions, the liquid flow rate was controlled by means of a peristaltic pump. In order to have a continuous flow rate in the test tube, a damping chamber was placed between the pump outlet and the inlet of the column.

The system was thermally insulated and the temperature difference, measured by thermocouples 1 and 2 (Fig. 1), was less than 0.3 °C. The liquid viscosity at the temperature of each experiment was measured using a Brookfield rotating viscometer. Care was taken to measure the viscosity of the glycerol solutions right after each set of experiments, in order to minimise water absorption and evaporation.

The test solutions were of water and aqueous glycerol, covering a range of viscosities from 1×10^{-3} to 1.50 Pa s.

2.2. Measurement techniques

The Taylor bubble velocity was measured by two laser diodes 0.25 m apart, mounted perpendicular to the tube and aimed at two photocells on the opposite side of the column. The signal yielded by each photocell drops abruptly when the bubble passes between the laser diode and the photocell. The bubble velocity was thus obtained; dividing the distance between the photocells by the time lag between their signal drop.

The PIV/PST technique consists of a board of light emitting diodes (LEDs) placed behind the test section, pulsing in synchronisation with a laser source, so that a CCD camera (PCO camera with a resolution of 1280 $(H) \times 1024$ (V) and 4096 grey levels) is able to acquire a frame containing both the seeding PIV particles and the bubble shadow. To obtain a close-up view of the flow in the liquid film, a 50 mm focal length lens was used. Fluorescent particles (orange vinyl pigment, 10 μm mean size) emitting light at 590 nm were used as seeding. The particles remained evenly dispersed in the test liquids after a day of testing.

A double-cavity pulsed Nd:Yag laser with a wavelength of 532 nm (pulse duration of 2.4 ns) and an adjustable pulse separation between each laser firing was used. The laser sheet had a thickness of about 1 mm in the test section. A red filter, opaque below 590 nm, was used to block the intense green laser reflections and to allow the passage of the light emitted by the fluorescent particles and by the LEDs. For more details see Nogueira et al. (2003).

The synchronisation between the laser, CCD camera and LEDs was made using a single signal generator. Each frame of the camera simultaneously recorded a LED pulse and a laser pulse. The resulting images had three different grey levels in descending order; corresponding to the seeding particles, background light and bubble shadow.

2.3. Data processing

The images recorded contained both the PST (bubble shape) and the PIV (flow field) information. The data processing was performed separately.

The flow field in the liquid was determined by processing the acquired images with the cross-correlation window displacement—iterative—multigrid algorithm (WIDIM), developed by Scarano and Riethmuller (1999). In this algorithm, the interrogation windows are displaced (according to the first vectors estimate) and their size is reduced iteratively. The use of a Gaussian interpolation function gives an estimate of the correlation peak location with sub-pixel accuracy. In this work, the initial image had 1280 $(V) \times 1024$ (H) pixels and the initial window size was 64×32 pixels, according to the flow direction. Two refinements were performed to reach the final interrogation windows of 16×8 pixels. An overlap of 50% refined the grid spacing to 8×4 pixels, which allowed a resolution of 0.342 mm × 0.171 mm ($0.01D \times 0.005D$) in the measurements around the bubble nose and a resolution of 0.138 mm × 0.069 mm ($0.04\delta \times 0.02\delta$, δ being the film thickness) in the annular liquid film. The time gap between the pulsing of the two laser cavities (pulse separation) was adjusted according to the measured velocities and varied from 120 to 2000 μs. The identification of spurious vectors was made, eliminating vectors with a signal-to-noise ratio (S/N) less than 1.5. Interpolated vectors from the adjacent ones neighbours replaced these spurious vectors. The average signal-to-noise (S/N) in a processed PIV image was around 10. Some erroneous vectors appeared inside the bubble, due to virtual particle images formed by refraction and reflection of the light emitted by the particles at the gas–liquid interface. The elimination of these vectors was possible since the simultaneous PIV and PST allows the determination of the exact position of the interface. The image processing to obtain the shadow of the bubble (and therefore the bubble shape) was performed in several steps, described in detail by Nogueira et al. (2003).

Tests made with known particle displacements showed a maximum uncertainty of 0.8 pixels in the liquid velocity around the bubble nose. This corresponds to a maximum relative error of 4% in the velocity around and ahead of the nose of the Taylor bubbles, for all the solutions studied and PIV times chosen.

3. Results and discussion

The flow fields ahead of the nose and in the annular region of individual Taylor bubbles rising through stagnant (S) and co-current (C) flowing liquids were determined. The viscosity of the liquids used varied in the range of 1×10^{-3} to 1.50 Pa s. The experimental conditions are summarised in Table 1. The bubble Reynolds number, Re_{U_∞}, is based on the bubble velocity U_∞ in stagnant conditions, and the film Reynolds number Re_{U_δ} is defined as $U_\delta \delta / v$, U_δ being the absolute mean velocity of the liquid in the stabilised (liquid) film of thickness δ.

The measured values of Taylor bubble velocity in stagnant conditions, U_B, are in very good agreement with those proposed by White and Beardmore (1962). For the experiments in co-current flow, the experimental values of U_B were compared with the predictions from Nicklin's equation (Nicklin et al., 1962):

$$U_B = cU_L + \alpha\sqrt{gD} = cU_L + U_\infty, \quad (1)$$

where U_L is the mean velocity of upward liquid flow in the tube and α is a parameter depending on the viscous, interfacial and inertial forces (White and Beardmore, 1962). Coefficient c takes values of around 1.2 when the liquid flow is turbulent and around 2.0 when it is laminar.

After measuring the rising velocity of the bubble, U_B, and the main liquid velocity, U_L, values of c were determined

Table 1
Experimental conditions (S—Stagnant; C—Co-current)

μ (Pa s)	ρ (kg/m^3)	T (°C)	U_B (m/s)	$\delta_{exp} \times 10^3$ (m)	Re_{U_∞}	U_L/U_∞	Re_{U_δ}	S/C
1.500	1262.0	19.7	0.120	5.14	3	0	0.5	S
0.205	1232.4	19.7	0.303	3.87	—	0.29	6	C
0.200	1232.8	20.4	0.188	3.84	37	0	6	S
0.190	1232.8	20.8	0.190	3.78	37	0	6	S
0.111	1222.2	20.2	0.197	3.29	69	0	12	S
0.109	1221.8	20.4	0.197	3.27	70	0	12	S
0.046	1201.9	19.8	0.226	2.48	—	0.07	33	C
0.045	1201.3	20.9	0.394	2.71	—	0.46	42	C
0.043	1199.9	21.3	0.197	2.40	177	0	34	S
0.043	1200.3	21.3	0.282	2.69	—	0.21	37	C
0.043	1200.3	21.3	0.364	2.67	—	0.37	43	C
0.028	1188.4	20.3	0.197	2.15	263	0	53	S
0.025	1183.4	19.2	0.197	2.19	296	0	59	S
0.025	1183.4	19.2	0.358	2.33	—	0.41	73	C
0.016	1169.0	19.2	0.251	—	—	0.14	—	C
0.016	1170.0	19.0	0.318	—	—	0.31	—	C
0.015	1168.0	20.2	0.209	1.87	—	0.03	105	C
0.014	1169.9	21.8	0.197	1.84	511	0	106	S
0.014	1170.0	21.9	0.272	—	—	0.20	—	C
0.014	1169.7	21.8	0.358	2.39	—	0.40	130	C
0.014	1170.0	21.8	0.378	2.58	—	0.51	116	C
0.005	1120.7	22.0	0.197	1.54	1315	0	282	S
0.004	1099.1	23.1	0.197	1.51	1881	0	405	S
0.003	1086.3	22.2	0.197	1.49	2504	0	540	S
0.002	1070.2	19.9	0.268	1.89	—	0.18	661	C
0.002	1071.4	18.4	0.197	1.62	2826	0	603	S
0.001	1000.0	22.3	0.197	1.17	6293	0	1403	S

from Eq. (1) as

$$c = \frac{U_B - \alpha\sqrt{gD}}{U_L}. \tag{2}$$

The obtained values are very close to the value of 2.0, which is predictable for laminar regime in the liquid.

The liquid velocity just ahead of the bubble nose (a stagnation region in a reference frame attached to the bubble) should be identical to the bubble velocity. For all the conditions studied, the liquid velocities measured just ahead of the nose are around 3% above U_B, which is a value lower than the experimental velocity uncertainty.

Fig. 2 shows the liquid flow field ahead of a Taylor bubble rising in a stagnant glycerol solution ($\mu = 0.19$ Pa s) in a fixed frame of reference (a), and in a reference attached to the bubble (b). The vectors correspond to only one out of seven vectors to help visualisation of the flow. The axial coordinate z is taken relative to the nose of the bubble, and it is positive downwards. The shape of the bubble, which is simultaneously determined, is also represented. As depicted in the figures, the gas slug displaces the liquid ahead of it, and the vectors near the interface and slightly below the nose show a strong radial component. As the liquid film thickness decreases the axial liquid velocity increases, thereby insuring a constant volumetric flow rate. The maximum liquid velocity in the axial direction in a given cross-section approaches the gas–liquid interface, and the liquid film thickness, δ, tends to become constant. The equilibrium between the weight of each infinitesimal fluid element and the viscous forces acting on its boundaries is then reached, and the flow in the liquid film becomes fully developed.

3.1. Flow in the nose region of the Taylor bubble

Fig. 3 shows instantaneous liquid velocity profiles ahead of a Taylor bubble rising through a stagnant aqueous glycerol solution ($\mu = 0.20$ Pa s). The presence of the bubble is 'felt' for some distance ahead of the nose. Values for the distance until where the flow is disturbed by the presence of the bubble were determined in a dimensionless form, Z'/D, for all the conditions studied, using the following method:

- For seven radial positions and different axial distances ahead of the bubble nose, the axial velocity component was extracted from the velocity profile.
- For each radial position, the square of the deviation between the local value of the axial velocity and the value for the same radial position far ahead ($3D$) of the bubble was determined. The variable R, equal to the square root of the mean squared deviation (sum of the seven squared deviations divided by seven), was then computed and represented as a function of the axial dimensionless distance from the bubble nose, as shown in Figs. 4(a) and (b) for

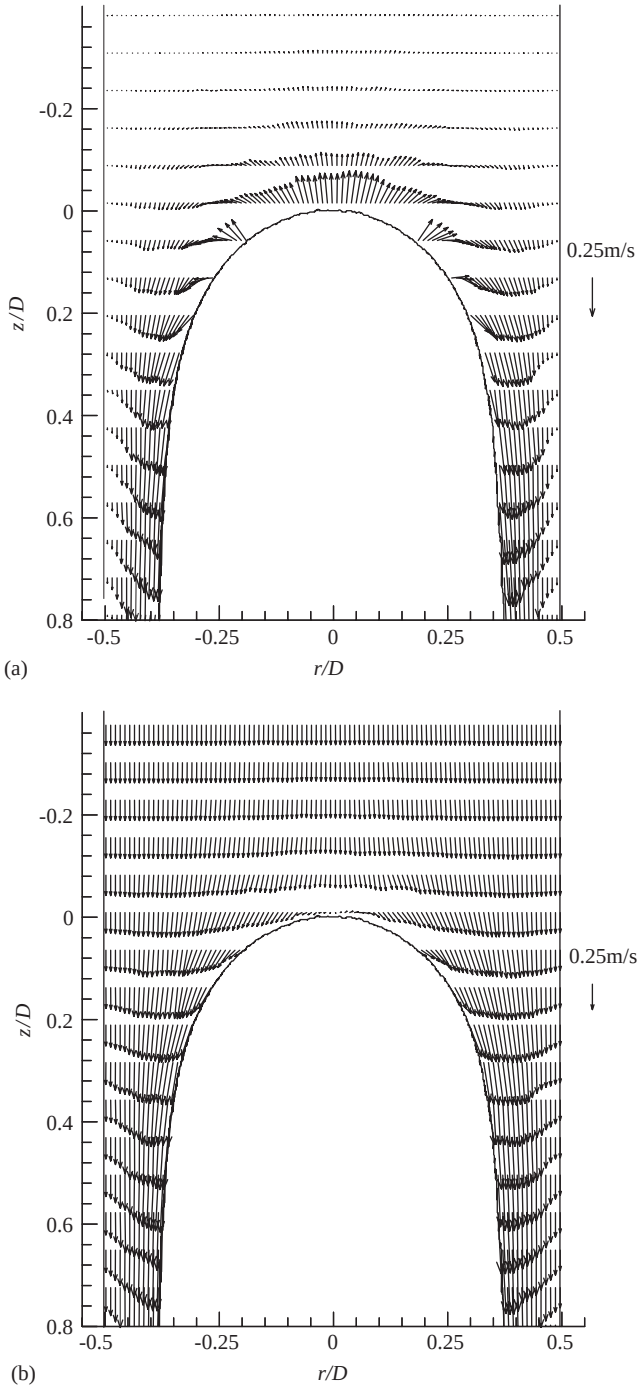

Fig. 2. Velocity profile around the nose of a Taylor bubble rising in a stagnant solution with $\mu = 0.109$ Pa s (a) in a fixed frame of reference and (b) in a frame of reference moving with the bubble.

stagnant and co-current flowing conditions, respectively. The axial distance from the nose at which R reaches a constant value (very close to zero) is the required value of Z'/D.

- For each experiment, in both stagnant and co-current flow conditions, the velocity profile unaffected by the bubble was obtained from the PIV images at a distance of around $3D$ ahead of the bubble nose.

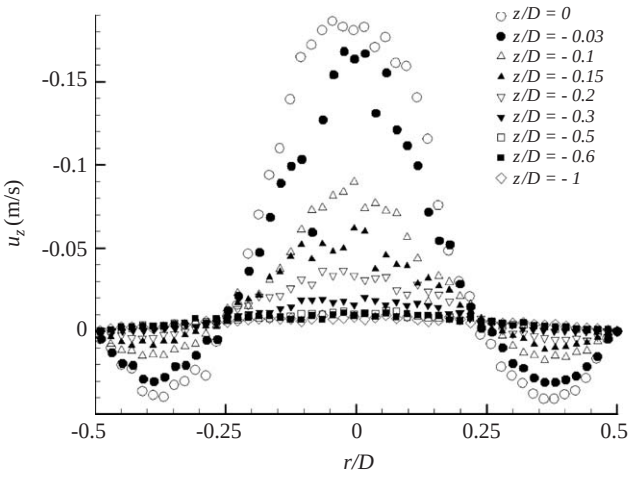

Fig. 3. Axial velocity profiles in a fixed frame of reference for different distances ahead of the bubble nose for a Taylor bubble rising in a stagnant solution with $\mu = 0.200$ Pa s.

Fig. 5 shows the values of Z'/D for the different conditions studied as a function of the bubble Reynolds number, Re_{U_∞}. For stagnant conditions (dark symbols), the absolute values of Z'/D slightly increase for decreasing liquid viscosities, suggesting that the presence of the bubble is felt slightly further away, as the inertial forces are higher relative to the viscous ones. The absolute values of Z'/D also increase for increasing mean liquid velocities (open symbols). In a reference frame attached to the bubble, the higher the values of U_L are, the higher are the values of the downward liquid flow rates. These increasing liquid flow rates justify the higher Z'/D values observed. The value of $Z' = 0.35D$ obtained for pure glycerol compares well with the value of $Z' = 0.3D$ obtained by Bugg and Saad (2002) in their experiments with kerosene. Polonsky et al. (1999) and van Hout et al. (2002) report values of $0.66D$ and $0.55D$ for bubbles rising in stagnant water. As far as the authors are aware, there are no values reported for Z'/D in co-current conditions in the literature.

Dumitrescu (1943) was the first to study an individual bubble rising in a stagnant liquid. He derived, from potential flow, a Taylor bubble shape that agrees very well with experimental data (Mao and Dukler, 1991) for air–water systems.

Dumitrescu's shape profile was divided into two regions, the nose region and the film region:

$$\left(\frac{z}{D}\right) = 0.375\left[1 - \sqrt{1 - 7.112\left(\frac{r}{D}\right)^2}\right]$$

$$\text{when } \left(\frac{z}{D}\right) \leqslant 0.25, \tag{3a}$$

$$\left(\frac{z}{D}\right) = \frac{0.0615}{(1 - 4(r/D)^2)^2} \quad \text{when } \left(\frac{z}{D}\right) \geqslant 0.25. \tag{3b}$$

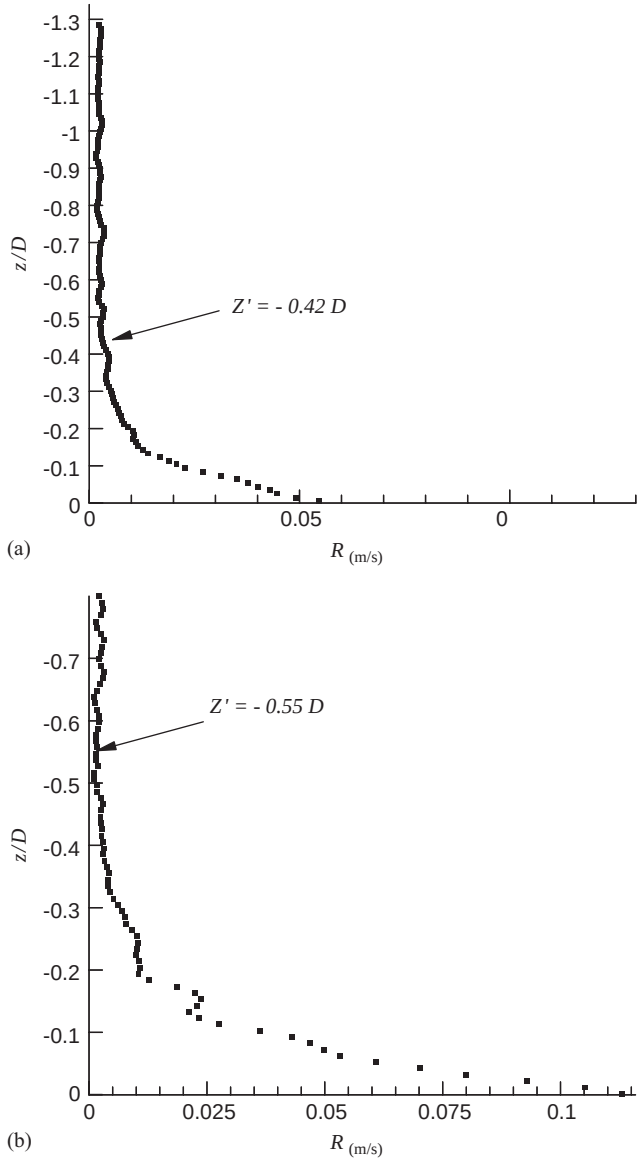

Fig. 4. Representation of variable R along the axial distance from the bubble nose, for experiments in stagnant flow conditions (a) μ=0.200 Pa s and (b) $\mu = 0.109$ Pa s.

The obtained shapes for the nose region are presented in Figs. 6(a)–(d). In Fig. 6(a) the bubble shapes are plotted for stagnant conditions and different liquid viscosities (1×10^{-3} Pa s $< \mu <$ 1.5 Pa s). The curvature of the nose (in the vertical plane containing the column axis) is lower for higher viscosities, evidence of the increasing influence of the viscous forces. Figs. 6(b) and (c) show the shapes of Taylor bubbles rising through aqueous glycerol solutions with viscosities of 0.015 and 0.043 Pa s, respectively, corresponding to inertial controlled regime (according to White and Beardmore, 1962). For both solutions, the curvature radius is lower for the higher bubble velocities in order to accommodate the higher liquid flow rates coming downwards (reference frame attached to the bubble).

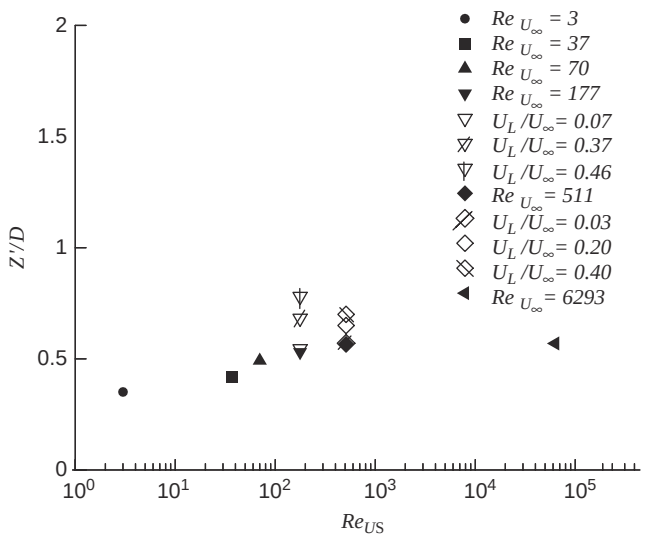

Fig. 5. Representation of the values of Z'/D as a function of Re_{U_∞} for stagnant conditions (open symbols) and for co-current flow conditions (full symbols).

The experimental shapes for stagnant flow conditions are compared in Fig. 6(d) with Dumitrescu's profile for potential flow, according to Eqs. (3a) and (3b). The Taylor bubble shapes approximate this theoretical profile as the viscosity decreases, and is in excellent agreement for water.

3.2. Flow in the developing and stabilised film

Fig. 7 shows an instantaneous liquid velocity profile in the developing film region around a Taylor bubble rising in a stagnant aqueous glycerol solution ($\mu = 0.19$ Pa s) in a fixed frame of reference. When the velocity profile becomes fully developed the film thickness (δ) becomes constant. The distance from the bubble nose at which the liquid film reaches a constant thickness, Z^*, as well as the thickness δ of the stabilised film are important parameters to determine. The flow pattern in the wake of the Taylor bubble is expected to be independent of the bubble length for lengths greater than Z^*, and strongly dependent on δ (the film thickness).

In Figs. 8(a) and (b) instantaneous axial (u_z) and radial (u_r) components of the liquid velocity along the annular film are represented for a radial position of $r/D = 0.44$ for (a) stagnant conditions, and of $r/D = 0.42$ for (b) co-current conditions (both radial positions are approximately at the middle of the stabilised films). As before, the origin of the axial coordinate z is taken at the bubble nose. In the figures the average values of u_z, $u_{z_{av}}$, calculated with all the data between each axial position and around $4D$ to $6D$ downwards, are also plotted. These data were obtained from several consecutive PIV images 'stitched' together in order to have the entire film.

The axial velocity component increases along the film until it becomes fully developed, i.e., until it reaches a constant thickness. From the axial velocity component, values

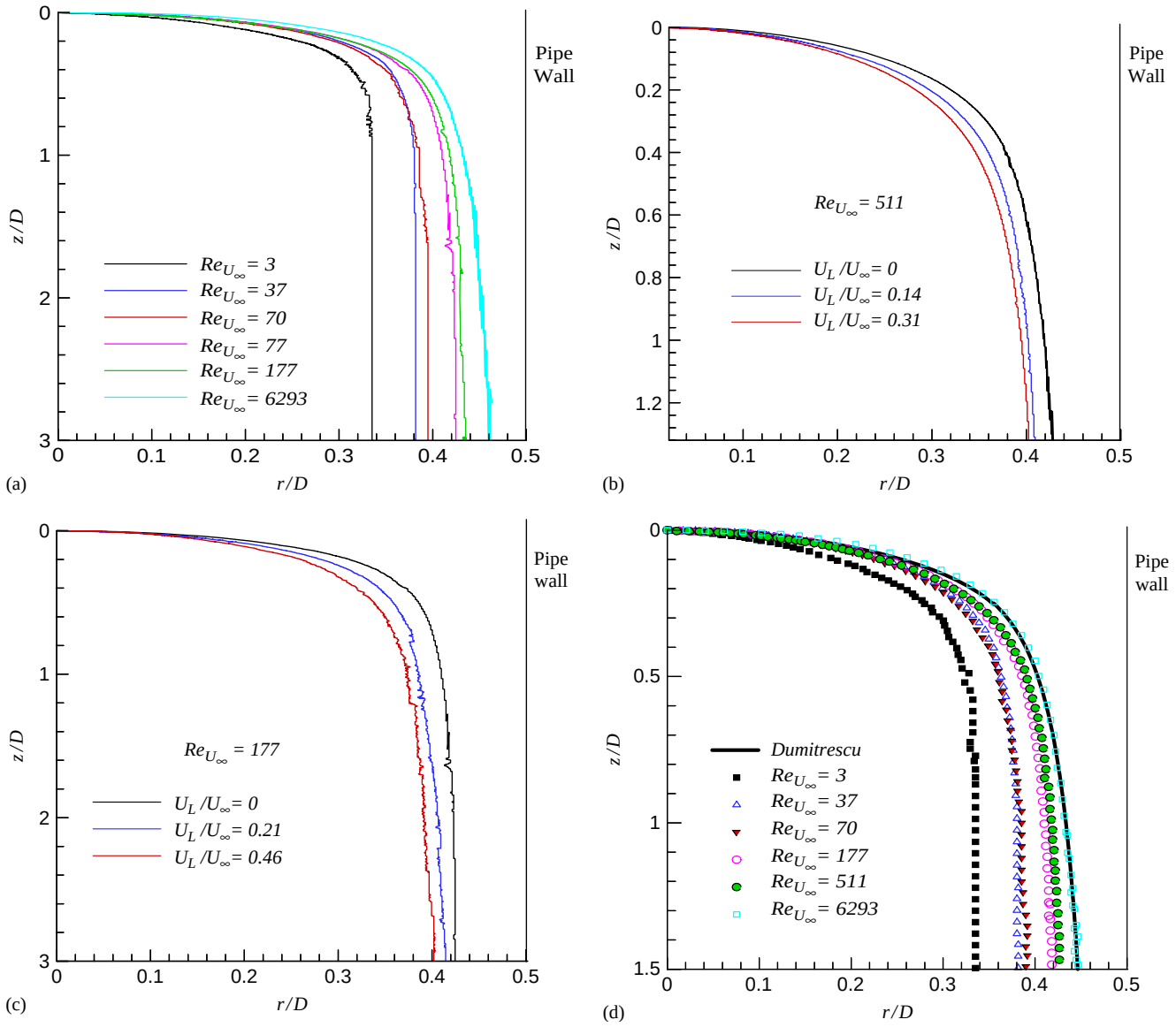

Fig. 6. (a) Experimental shape of the Taylor bubble in the nose region for stagnant conditions; (b) experimental shape of the Taylor bubble in the nose region for co-current conditions ($\mu = 0.015$ Pa s); (c) experimental shape of the Taylor bubble in the nose region for co-current conditions ($\mu = 0.043$ Pa s); (d) comparison between experimental shapes and Dumitrescu's shape profile for stagnant conditions.

for the length of the developing film (Z^*) were estimated: about $2.2D$ for stagnant liquid and about $3.6D$ for co-current flowing liquid (for the experiments represented in the figure). The radial component of the film velocity reaches a value around zero (fully developed film) for the same values of Z^*. Similar developing lengths were found analysing the values of $u_{z_{av}}$, since they reach a constant value for the same values of Z^*.

A theoretical estimate of the length Z^* for which the boundary layer from the wall reaches the free streamline along the bubble interface, as reported by Campos and Guedes de Carvalho (1988), can be given by

$$\frac{Z^*}{D} \approx \frac{[(g\delta^2/2\nu) + U_B]^2}{2gD}, \tag{4}$$

where g is the acceleration due to gravity and ν is the kinematic viscosity. This equation was deduced supposing unidirectional flow in a liquid layer with a free surface in a two-dimensional vertical wall, and applying Bernoulli's equation along the free surface streamline.

In Fig. 9, the ratio between experimental values of Z^*/D and the predictions of Eq. (4) is represented against the film Reynolds number, based on the absolute mean velocity in the liquid film (U_δ) and on the film thickness (δ) for the conditions studied. As depicted in the figure, Eq. (4) under-predicts the film developing length for low values of Re_{U_δ}. This is due to the hypothesis of potential flow in the deduction of Eq. (4). For intermediate values of Re_{U_δ} the theory seems to well predict the developing length. Above values of Re_{U_δ} around 80, the experimental values are lower

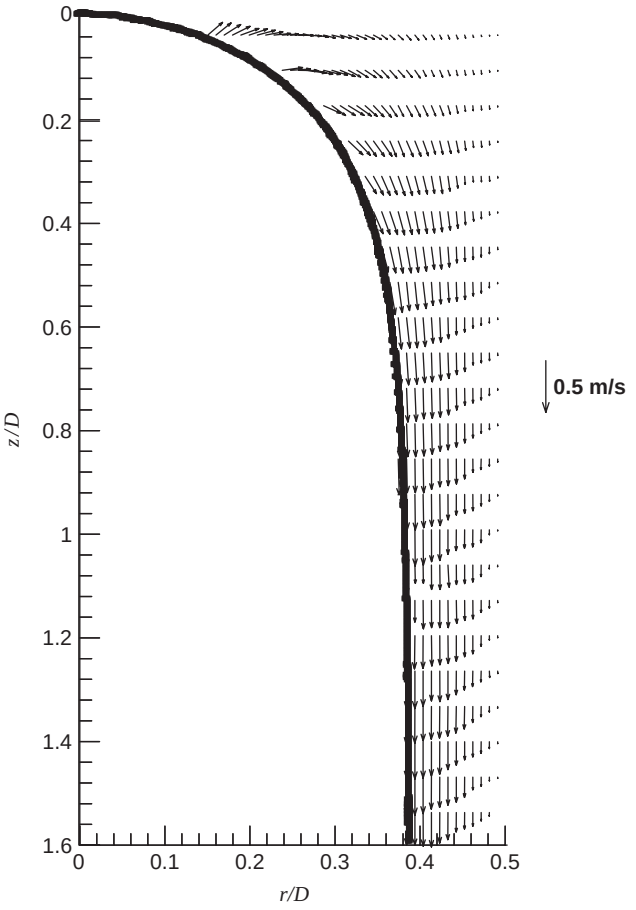

Fig. 7. Velocity profile in the developing film region around a Taylor bubble in stagnant liquid ($\mu = 0.190$ Pa s) in a fixed frame of reference.

than the predictions, which might indicate the transition from laminar to turbulent regime in the film flow.

Brown (1965) theoretically deduced an expression for the velocity profile in a stabilised free-falling laminar film around a Taylor bubble rising trough a co-current flowing liquid (mean liquid velocity U_L):

$$u_z = \frac{g}{v}\left[\frac{R^2 - r^2}{4} - \frac{(R-\delta)^2}{2}\ln\frac{R}{r}\right], \tag{5}$$

where the film thickness (δ) is given by

$$\delta = \left[\frac{3v}{2g(R-\delta)}((R-\delta)^2 U_B - R^2 U_L)\right]^{1/3}. \tag{6}$$

This equation was obtained by applying a material balance, in a reference moving with the bubble, between a plane far ahead of the bubble nose and a plane located at the fully developed film, giving

$$Q_v = (U_B - U_L)\pi R^2 = \int_{R-\delta}^{R} (u_z + U_B) 2\pi r \, \mathrm{d}r, \tag{7}$$

where Q_v is the volumetric liquid flow rate in a reference moving with the bubble.

In the absence of friction at the free gas–liquid interface, the wall shear stress (τ_w) supports the total body force on the film, so that

$$\tau_w = \frac{\delta(2R-\delta)}{2R}\rho g, \tag{8}$$

for cylindrical geometry.

Assuming a plane wall geometry ($\delta/D \ll 1$), Eq. (6) can be simplified, yielding

$$\delta = \left[\frac{3vR}{2g}(U_B - U_L)\right]^{1/3}. \tag{9}$$

For this case, the mean absolute liquid velocity in the film (U_δ) is given by

$$U_\delta = \frac{g\delta^2}{3v}. \tag{10}$$

The film Reynolds number (Re_{U_δ}) is defined as

$$Re_{U_\delta} = \frac{Q_v}{v\pi D} \tag{11}$$

after combining Eqs. (7) and (9).

Figs. 10(a) and (b) show the average developed velocity profiles in the annular film for the stagnant conditions ($U_L = 0$) and co-current conditions studied, respectively. The experimental profiles represent the average of 60 instantaneous profiles along the stabilised film. The lines represent, for each experiment, the theoretical laminar profile given by Eq. (5) with the film thickness predicted by Eq. (6). For each value of Re_{U_δ}, the average experimental profile is plotted within the film thickness determined from the bubble shadow. The values of Q_v, needed to compute Re_{U_δ}, were calculated by integration of the experimental velocity data, and are in close agreement with those predicted from Eqs. (5)–(7). The experimental profiles compare well (mean deviations under 5%) with the predictions from Brown's equation for low values of Re_{U_δ}. The deviations are particularly significant (more than 50%) for the highest value of the film Reynolds number. A similar conclusion arises from the comparison between the experimental values of the film thickness and the predictions from Eq. (6). For low values of Re_{U_δ}, Eq. (6) predicts the film thickness very well (deviations below 3%), while for values of Re_{U_δ} greater than around 80, the deviations become greater than 30%, suggesting the onset of flow transition in the film. The plot of Fig. 11 gives evidence of this feature. The transition from laminar to turbulent regime might start at values of Re_{U_δ} around 80, since from there on the ratio between the experimental values of δ and the predictions from Eq. (6) becomes significantly different from 1.0.

Fulford (1964) reports the results of different investigators, concerning the critical film Reynolds number at which the turbulence in a falling film starts. Several of these studies have quoted upper and lower critical values enclosing the transition region. In spite of a reasonable scattering of

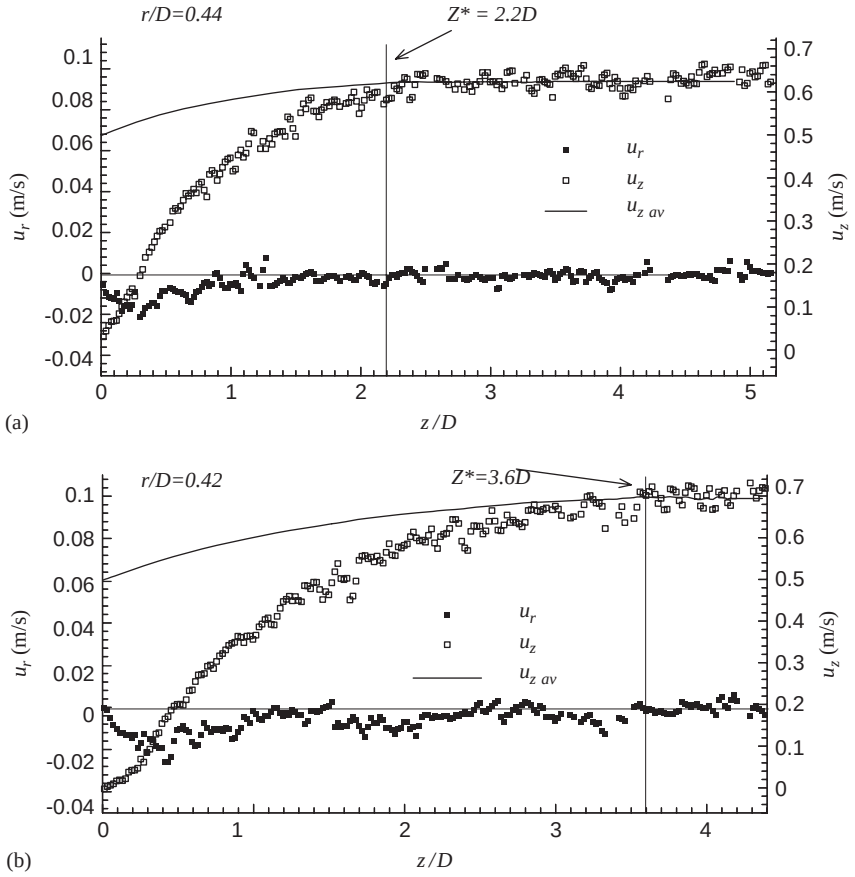

Fig. 8. (a) Axial, radial and average axial components of the velocity in the liquid film for stagnant conditions ($\mu = 0.043$ Pa s); (b) axial, radial and average axial components of the velocity in the liquid film for co-current conditions ($\mu = 0.043$ Pa s).

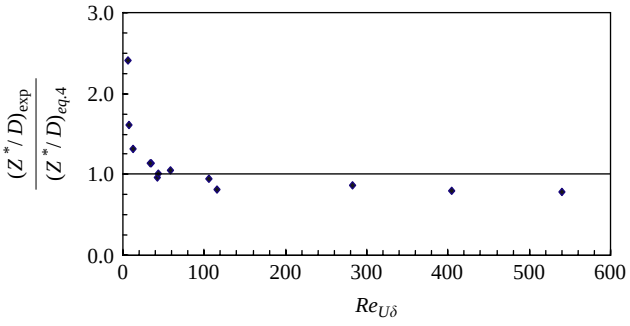

Fig. 9. Comparison between experimental values of Z'/D and theoretical predictions from Eq. (4).

the reported values, the bulk of evidence seemed to support a lower value of the critical Reynolds number in the region of 250–400 (a few studies reported values around 100–140), and a less well-defined upper value of about 800.

Because of the great complexity of turbulent flow in thin films, information on this is scarce in the literature. Von Kármán (1939) suggested the existence of a universal velocity profile for single-phase turbulent flow in a smooth pipe in terms of two parameters (neglecting free surface oscillations):

$$u^+ = \frac{u_z}{u^*}, \tag{12}$$

$$y^+ = \frac{u^* y}{\nu}, \tag{13}$$

where y is the distance from the wall and the friction velocity, u^*, is defined as

$$u^* = \left(\frac{\tau_w}{\rho}\right)^{1/2}. \tag{14}$$

In his data, Nikuradse (1933) verified this universal profile and demonstrated the existence of a buffer region between the laminar sub-layer and the main turbulent stream. The equations and limits of application suggested by Nikuradse and presented by Duckler and Bergelin (1952) are

$$u^+ = y^+ \quad \text{for } 0 \leqslant y^+ \leqslant 5 \text{ (laminar sub-layer)}, \tag{15}$$

$$u^+ = -3.05 + 5.0 \ln y^+ \quad \text{for } 5 < y^+ \leqslant 30 \text{ (buffer layer)}, \tag{16}$$

$$u^+ = 5.5 + 2.5 \ln y^+ \quad \text{for } 30 < y^+ \leqslant b^+ \text{ (turbulent zone)}, \tag{17}$$

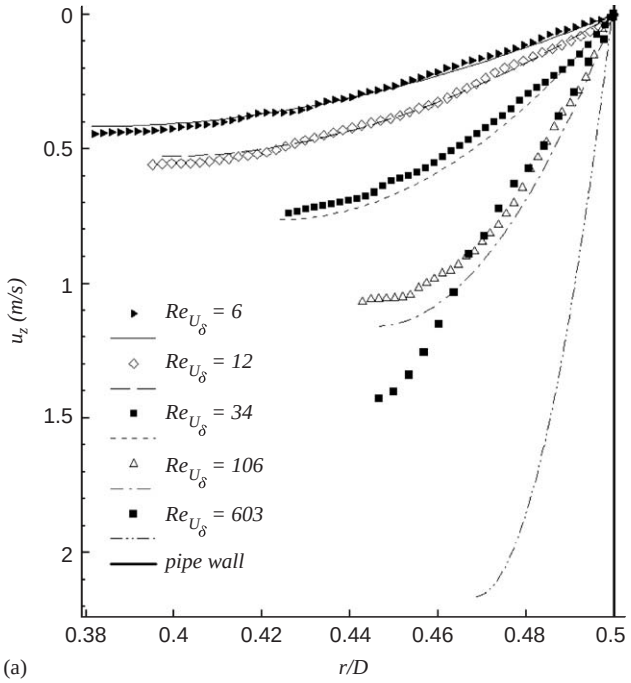

(a)

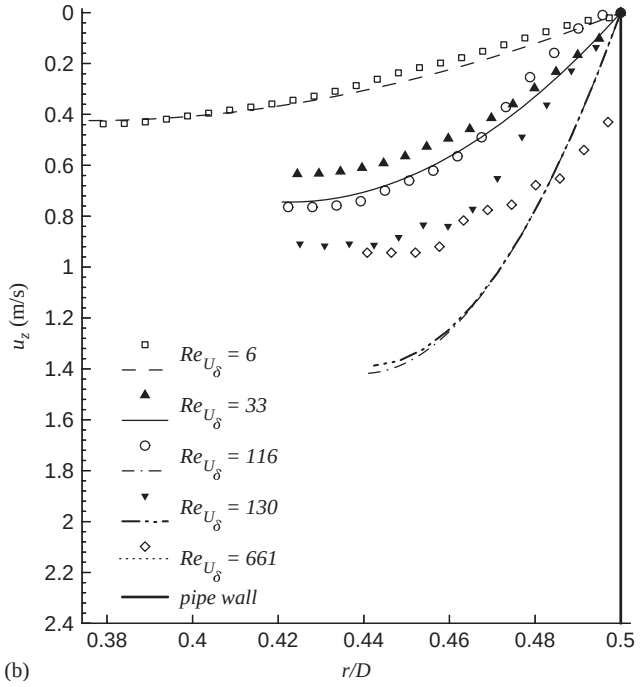

(b)

Fig. 10. (a) Average of the axial component of the velocity in the fully developed film, for the conditions studied with stagnant liquid in the pipe. The lines correspond to the theoretical predictions from Brown's equation (Eq. (5)); (b) average of the axial component of the velocity in the fully developed film, for the conditions studied with co-current flowing liquid in the pipe. The lines correspond to the theoretical predictions from Brown's equation (Eq. (5)).

where b^+ is defined by

$$b^+ = \frac{u^* \delta}{\nu}. \tag{18}$$

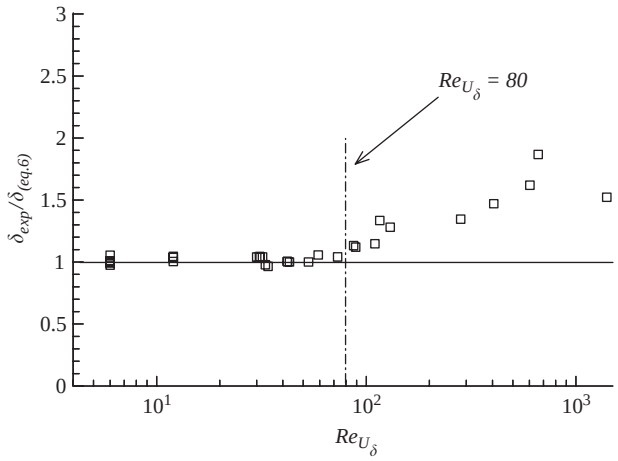

Fig. 11. Comparison between experimental values of the developed film thickness and predictions from Eq. (6).

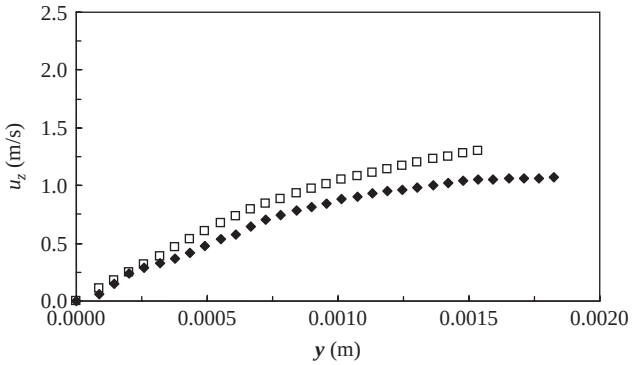

Fig. 12. Comparison between the experimental average velocity profiles (full symbols) in the stabilised film and theoretical predictions (open symbols) from Eqs. (12)–(17) for turbulent flow.

In Fig. 12, the axial velocity profile in the stabilised film (for $Re_{u_\delta} = 106$ and stagnant conditions) extracted from Fig. 10(a) is compared with the theoretical predictions (open symbols) from Eqs. (12) to (17) for turbulent film flow. The values of the predicted axial velocity in the film are calculated using the wall shear stress, τ_w, given by Eq. (8). The film thickness in Eqs. (8) and (18) was obtained by an iterative procedure integrating the theoretical velocity profile, until the experimental volumetric liquid flow rate Q_v (in a reference moving with the bubble) was obtained (Eq. (7)).

The results compare reasonably well with the predictions, especially just near the wall in the laminar sub-layer. The deviations, always lower than 20%, are more significant in the buffer zone near the gas–liquid interface where some shear stress may occur. For this experimental condition the predicted value for the dimensionless film thickness, $b^+ = 15.7$, suggests the inexistence of the main turbulent layer occurring for $b^+ > 30$.

The determination of the shear stresses along the annular film can also be performed from the velocity data obtained.

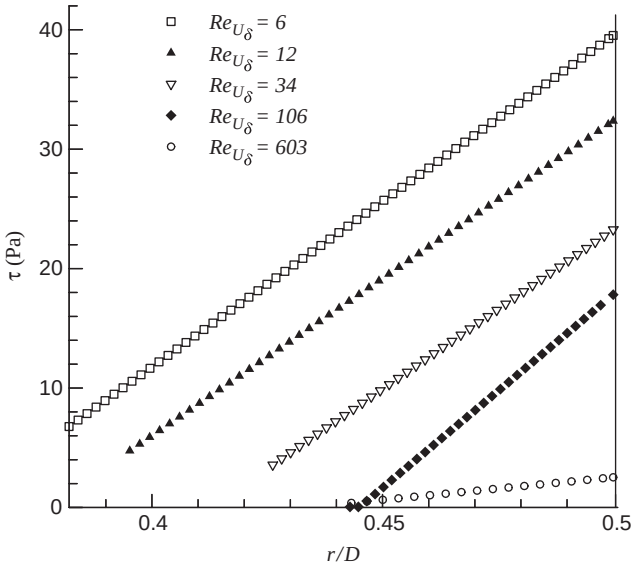

Fig. 13. Shear stress profile in the developed liquid film around Taylor bubbles rising in stagnant liquids.

This information is important, since data is scarce in the literature.

In Fig. 13, the shear stress profile is plotted for the stagnant liquid conditions. The experimental values of the shear stress along the film were obtained from the averaged fully developed velocity profiles presented in Fig. 10(a).

The results show a decrease in the shear stresses for decreasing liquid viscosities (higher values of Re_{U_δ}). For the laminar regime, the linearity of the shear stress profiles was expected, because the liquid velocity profile (Eq. (5)) is a second-order velocity profile since the parcel with the logarithm is negligible. The obtained values of the interface shear stresses are low, confirming the generally accepted assumption of null interfacial shear stress.

Figs. 14(a) and (b) show the shear stress profile in the film around Taylor bubbles rising through aqueous glycerol solution with viscosities 0.043 and 0.015 Pa s, respectively, obtained in stagnant ($U_L/U_\infty = 0$) and co-current flow conditions ($U_L/U_\infty \neq 0$). For the most viscous solution the shear stress profiles are almost coincident, meaning that the influence of the liquid flow rate is not significant. For the less viscous solution, however, the increase of the stabilised film thickness for increasing liquid flow rates leads to a lower mean velocity in the film and a lower velocity gradient at the wall. Once again, the values of the shear stress at the gas–liquid interface are very low.

Finally, in Fig. 15, the values of the wall shear stress are represented versus Re_{U_δ} for all the conditions studied. A general tendency for decreasing wall shear stress with increasing Re_{U_δ} is evident from the plot of the figure. The experimental values are in accordance (deviations under 5%) with the wall shear stresses predicted from Eq. (8), with the exception of the value around 3 Pa obtained for the more dilute solution ($\mu = 0.002$ Pa s). However, this value agrees

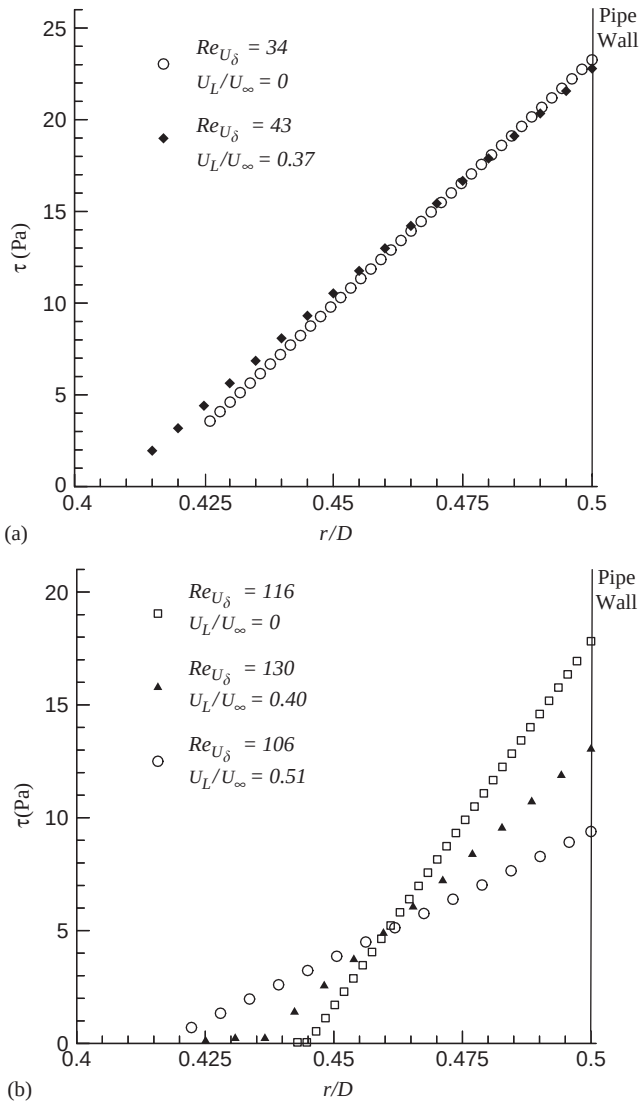

Fig. 14. (a) Shear stress profile in the developed liquid film around Taylor bubbles rising in aqueous glycerol solutions ($\mu = 0.043$ Pa s) obtained in stagnant ($U_L/U_\infty = 0$) and co-current ($U_L/U_\infty \neq 0$) conditions; (b) shear stress profile in the developed liquid film around Taylor bubbles rising in aqueous glycerol solutions ($\mu = 0.015$ Pa s) obtained in stagnant ($U_L/U_\infty = 0$) and co-current ($U_L/U_\infty \neq 0$) conditions.

reasonably well with reported values by Nakoryakov et al. (1986) and Mao and Dukler (1991) for similar conditions. The values of shear stress in the film presented are important for the simulation of processes such as depolarisation by slug flow in tubular separation membranes (Taha and Cui, 2002).

4. Conclusions

The flow in the nose region and in the annular film around individual Taylor bubbles rising through stagnant and co-current vertical columns of liquid was studied employing a non-intrusive technique, particle image velocimetry (PIV)

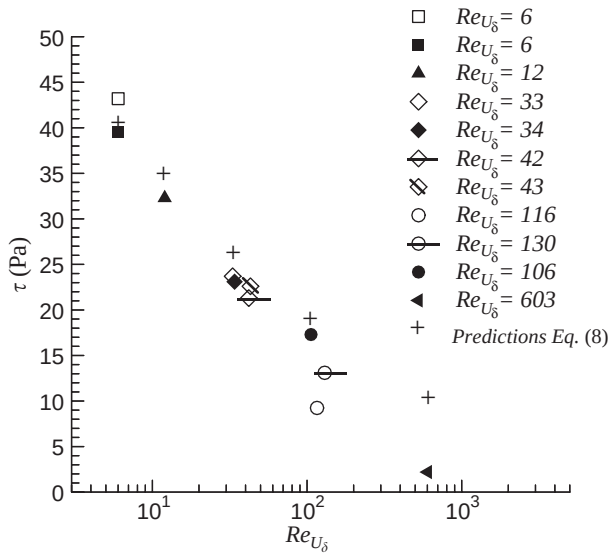

Fig. 15. Wall shear stresses as a function of Re_{U_δ}. The crosses represent the wall shear stress predictions from Eq. (8) for the experiments in stagnant conditions.

and pulsed shadowgraphy techniques (PST) simultaneously. This combined technique allows the simultaneous determination of the bubble interface shape from the PST, as well as the velocity profiles in the liquid film and nose region from the PIV.

Values for the distance ahead of the nose for which the liquid is disturbed by the presence of the bubble are presented for the conditions studied, showing that this distance is low, for both stagnant and co-current flow conditions. The longer distances are for low liquid viscosities and high liquid flow rates.

Bubble shapes in the nose region are presented and compared to Dumitrescu's theoretical predictions supposing potential flow. The shape profiles approximate the theory as the liquid viscosity decreases, and are in excellent agreement with experiments in water.

The velocity profiles near the nose region indicate accelerating flow in the initial stages of the falling film formation. Further downwards the velocity profiles are those of a developed falling film, and the thickness of the film is constant. This result is in contrast with the findings several authors obtained with intrusive techniques (Mao and Dukler, 1991).

Values for the dimensionless developing film length are reported and compared with theoretical predictions supposing potential flow in the nose region. For values of the Reynolds number based on the mean absolute velocity in the liquid film, Re_{U_δ}, greater than around 80, the experimental values for the developing length become lower than the predictions, suggesting that transition from laminar to turbulent regime occurs. Accordingly, the experimental velocity profiles are characteristic of developed laminar falling film until values of Re_{U_δ} around 80. The determined experimental values for the film thickness are also well predicted by laminar falling film theory in the same range of Re_{U_δ}. A value for the critical Reynolds number, Re_{U_δ}, around 80 is suggested from the present study, where a non-intrusive and accurate experimental technique was used.

An attempt was made to compare the experimental velocity profiles in the fully developed film for a value of $Re_{U_\delta} > 80$ with the universal velocity profile for single-phase turbulent flow proposed by Von Kármán and adapted to turbulent film flow by Duckler and Bergelin (1952). The experimental results compare reasonably well with the predictions, especially at the wall in the laminar sub-layer, showing significant deviations in the buffer zone near the interface.

Finally, the shear stress profile in the fully developed film was obtained for the conditions studied. The results show a decrease of the shear stresses for decreasing liquid viscosities. The influence of the liquid flow rate on the shear stresses is more significant for low viscosities. The lower values of the wall shear stresses were obtained for the higher liquid flow rates. For all the conditions, the values of the gas–liquid interfacial shear stress were low.

As shown in the present work, the nose shape, film thickness and wall shear stress are strongly influenced by viscosity, therefore this property is expected to play an important role in slug flow processes involving heat and mass transfer.

The data reported are relevant for the validation of numerical codes in slug flow.

Notation

b^+	dimensionless film thickness (Eq. (15)), m
c	velocity coefficient (Eq. (1))
C	co-current conditions (Table 1)
D	internal column diameter, m
g	acceleration due to gravity, m s^{-2}
H	number of pixels in the horizontal direction
Q_v	volumetric flow rate in a reference moving with the bubble, m^3 s^{-1}
r	radial position, m
R	internal column radius (Eqs. (5) and (6)), m or mean velocity deviation, m s^{-1}
S	stagnant conditions (Table 1)
u^+	normalised velocity (Eq. (12))
u^*	friction velocity (Eq. (14)), m s^{-1}
u_r	radial component of the velocity, m s^{-1}
u_z	axial component of the velocity, m s^{-1}
$u_{z_{av}}$	average value of u_z below an axial position, m s^{-1}
U_B	Taylor bubble velocity, m s^{-1}
U_L	mean superficial liquid velocity, m s^{-1}
U_∞	velocity of an individual bubblerising in a stagnant liquid, m s^{-1}
U_δ	liquid average velocity in the film relative to the tube wall, m s^{-1}

V	number of pixels in the vertical direction
y	distance from the wall, m
y^+	dimensionless distance from the wall, $y^+ = u^* y/\nu$
z	distance from the Taylor bubble nose, m
Z'	distance from the Taylor bubble nose for which the annular the flow is disturbed by the presence of the bubble, m
Z^*	distance from the Taylor bubble nose for which the annular liquid film stabilises or film developing length, m

Dimensionless groups

Re_{U_δ}	Reynolds number based on the mean absolute velocity in the liquid film ($=u_\delta \delta/\nu$)
Re_{U_∞}	Reynolds number based on the velocity of an individual bubble rising in a stagnant liquid ($=U_\infty D/\nu$)
$\frac{U_L}{U_\infty}$	velocity ratio
$\frac{Z'}{D}$	dimensionless distance from the nose where the flow is disturbed by the presence of the bubble
$\frac{Z^*}{D}$	dimensionless film developing length
$\left(\frac{Z^*}{D}\right)_{\text{exp}}$	experimental values of the dimensionless film developing length
$\left(\frac{Z^*}{D}\right)_{\text{Eq. (4)}}$	theoretical predictions of the dimensionless film developing length from Eq.(4)

Greek letters

α	parameter (Eq. (1)), m
δ	liquid film thickness, m
δ_{exp}	experimental values of the liquid film thickness, m
$\delta_{\text{Eq. (6)}}$	theoretical predictions of the liquid film thickness from Eq. (6), m
μ	liquid dynamic viscosity, Pa s
ν	liquid kinematic viscosity, $\text{m}^2\,\text{s}^{-1}$
ρ	liquid density, $\text{kg}\,\text{m}^{-3}$
τ	shear stress, Pa
τ_w	wall shear stress, Pa

Acknowledgements

The partial support of “Fundação para a Ciência e Tecnologia—Portugal” through project POCTI/EQU/33761/1999 is gratefully acknowledged: POCTI (FEDER) also supported this work via CEFT.

References

Brown, R.A.S., 1965. The mechanism of large bubbles in tubes. I. Bubble velocities in stagnant liquids. Canadian Journal of Chemical Engineering 43, 217–223.

Bugg, W., Saad, G.A., 2002. The velocity field around a Taylor bubble rising in a stagnant viscous fluid: numerical and experimental results. International Journal of Multiphase Flow 28, 791–803.

Campos, J.B.L.M., Guedes de Carvalho, J.R.F., 1988. An experimental study of the wake of gas slugs rising in liquids. Journal of Fluid Mechanics 196, 27–37.

Collins, R., De Moraes, F.F., Davidson, J.F., Harrison, D., 1978. The motion of a large gas bubble rising through liquid flowing in a tube. Journal of Fluid Mechanics 89, 497–514.

Duckler, A.E., Bergelin, O.P., 1952. Characteristics of flow in falling liquid films. Chemical Engineering Progress 48 (1), 557–563.

Dumitrescu, D.T., 1943. Strömung an einer Luftblase im Senkrechten Rohr. Zeitschrift fur Angewandte Mathematik und Mechanik 23, 139–149.

Fabre, J., Liné, A., 1992. Modeling of two-phase slug flow. Annual Review of Fluid Mechanics 24, 21–46.

Fernandes, R.C., Semiat, R., Dukler, A.E., 1983. A hydrodynamic model for gas–liquid slug flow in vertical tubes. A.I.Ch.E. Journal 29, 981.

Fulford, G.D., 1964. The flow of liquids in thin films. Advances in Chemical Engineering 5, 151–236.

Mao, Z.-S., Dukler, A., 1991. The motion of Taylor bubbles in vertical tubes. II—Experimental data and simulations for laminar and turbulent flow. Chemical Engineering Science 46, 2055–2064.

Moissis, R., Griffith, P., 1962. Entrance effects in a two-phase slug flow. Journal of Heat Transfer 84, 29–39.

Nakoryakov, V.E., Kashinsky, O.N., Kozmenko, B.K., 1986. Experimental study of gas–liquid slug flow in a small-diameter vertical pipe. International Journal of Multiphase Flow 12 (3), 337–355.

Nicklin, D.J., Wilkes, J.O., Davidson, J.F., 1962. Two-phase flow in vertical tubes. Transactions of the Institution of Chemical Engineers, 4061–4068.

Nikuradse, J., 1933. Laws of flow in rough pipes. Forschungsheft 361, 1.

Nogueira, S., Sousa, R.G., Pinto, A.M.F.R., Riethmuller, M.L., Campos, J.B.L.M., 2003. Simultaneous PIV and pulsed shadow technique in slug flow: a solution for optical problems. Experiments in Fluids 35, 598–609.

Pinto, A.M.F.R., Campos, J.B.L.M., 1996. Coalescence of two gas slugs rising in a vertical column of liquid. Chemical Engineering Science 51, 45–54.

Pinto, A.M.F.R., Coelho Pinheiro, M.N., Campos, J.B.L.M., 1998. Coalescence of two gas slugs rising in a co-current flowing liquid in vertical tubes. Chemical Engineering Science 53, 2973–2983.

Pinto, A.M.F.R., Coelho Pinheiro, M.N., Campos, J.B.L.M., 2001. On the interaction of Taylor bubbles rising in two-phase co-current slug flow in vertical columns. Experiments in Fluids 31, 643–652.

Polonsky, S., Shemer, L., Barnea, D., 1999. The relation between the Taylor bubble motion and the velocity field ahead of it. International Journal of Multiphase Flow 25, 957–975.

Scarano, F., Riethmuller, M.L., 1999. Iterative multigrid approach in PIV image processing with discrete window offset. Experiments in Fluids 26, 513–523.

Taha, T., Cui, Z.F., 2002. Hydrodynamic analysis of upward slug flow in tubular membranes. Desalination 145, 179–182.

van Hout, R., Gulitsky, A., Barnea, D., Shemer, L., 2002. Experimental investigation of the velocity field induced by a Taylor bubble rising in stagnant water. International Journal of Multiphase Flow 29, 579–596.

Von Kármán, T., 1939. The analogy between fluid friction and heat transfer. Transactions, American Society of Mechanical Engineers 61, 705.

White, E.T., Beardmore, R.H., 1962. The velocity of rise of single cylindrical air bubbles through liquids contained in vertical tubes. Chemical Engineering Science 17, 351–361.